Journal of Energy Storage 71 (2023) 108168

Contents lists available at ScienceDirect

Journal of Energy Storage

journal homepage: www.elsevier.com/locate/est

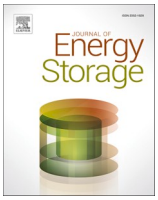

Research papers

Hierarchical spinel $NiMn_2O_4$ nanostructures anchored on 3-D nickel foam as stable and high-performance supercapacitor electrode material

Suprimkumar D. Dhas [a,c,1], Pragati N. Thonge [b], Shivaji D. Waghmare [c], Gopal K. Kulkarni [i], Surendra K. Shinde [d,h], Dae-Young Kim [d], Teja M. Patil [e], Manesh A. Yewale [f,1], Annasaheb V. Moholkar [g], Daewon Kim [a,*]

[a] Department of Electronic Engineering, Institute for Wearable Convergence Electronics, Kyung Hee University, 1732 Deogyeong-daero, Giheung-gu, Yongin 17104, South Korea
[b] School of Life Science, Punyashlok Ahilyadevi Holkar, Solapur University, Solapur, Maharashtra 416-004, India
[c] Department of Physics, Shri Shivaji Mahavidyalaya, Barshi, Maharashtra 413-401, India
[d] Department of Biological and Environmental Science, Dongguk University-Seoul, 32 Dongguk-ro, Ilsandong-gu, Goyang-si, 10326, Gyeonggi-do, South Korea
[e] Department of Physics, Bhogawati Mahavidyalaya Kurukali, Shivaji University, Kolhapur 416-004, Maharashtra, India
[f] School of Mechanical Engineering, Yeugnam University, Gyeongsan 38541, South Korea
[g] Thin Film Nanomaterials Laboratory, Department of Physics, Shivaji University, Kolhapur, Maharashtra 416-004, India
[h] Department of Physics, Art's, Science and Commerce collage Indapur, Maharashtra, 413-106, India
[i] Thick and Thin Film Device Laboratory, Department of Physics, Shivaji University, Kolhapur, Maharashtra, 416004, India

ARTICLE INFO

Keywords:
Energy storage
Hydrothermal
$NiMn_2O_4$-Ni foam electrode
Symmetric supercapacitors device

ABSTRACT

A simple hydrothermal route has been used to synthesize $NiMn_2O_4$ nanostructures (NSs) on nickel foam. The electrochemical investigation shows how annealing temperature affects its supercapacitive properties. The NMO@500-Ni-foam electrode shows a high specific capacitance of 930 Fg^{-1} at a constant scan rate of 5 mVs^{-1} in 1 M KOH electrolyte. Additionally, the corresponding symmetric supercapacitor device (SSCs) has a superior cyclic span with 93.7 % capacitance retention even after 5000 cycles, excellent electrochemical performance with a specific capacitance of 72.9 Fg^{-1}, specific energy of 11 $Whkg^{-1}$, and specific power of 857 Wkg^{-1}. The exceptional results suggest that $NiMn_2O_4$ grown on Ni-foam might be a promising candidate for electrochemical energy storage applications.

1. Introduction

The need for innovative energy know-how and conversion/storage initiatives has grown in recent years in order to address the world's pressing energy-related concerns as well as the current energy crises and environmental contamination [1–4]. To address this serious problem, there is an urgent need to develop energy-storage devices with high energy productivity, long lifespans, and exceptional chemical stability [5–7]. Supercapacitors (SCs), a type of energy storage system, have drawn the attention of researchers because of their exceptional features like quick charging and discharging, high power density, and environmental friendliness. But the energy density is lower than anticipated. The development of effective electrode materials can aid in the resolution of such issues [8–10].

Metal oxides of the spinel type have shown promise in a number of fields, including energy storage and conversion. Spinel-type metal oxides with the structural formula AB_2O_4 have drawn a interest as prospective energy storage materials because of their high theoretical capacitance, wide availability, and inexpensive cost [11–12]. In addition, transition metal oxides (TMOs) such as $NiCo_2O_4$, $NiFe_2O_4$, $ZnCo_2O_4$, $MnFe_2O_4$, and $NiMn_2O_4$ have sparked increased interest in energy storage due to their remarkable synergistic influence on the existence of two distinct cations in a mono crystalline phase, which can improve chemical stability and electrochemical performance of binary metal NPs [13–17]. The most appealing choice is $NiMn_2O_4$, which has a higher capacity for charge storage and higher conductivity than pure nickel and manganese oxide.

Additionally, the lattice orientations, including Mn and Ni, may offer

* Corresponding author.
E-mail address: daewon@khu.ac.kr (D. Kim).
[1] Equal contribution.

https://doi.org/10.1016/j.est.2023.108168
Received 18 February 2023; Received in revised form 19 June 2023; Accepted 20 June 2023
Available online 6 July 2023

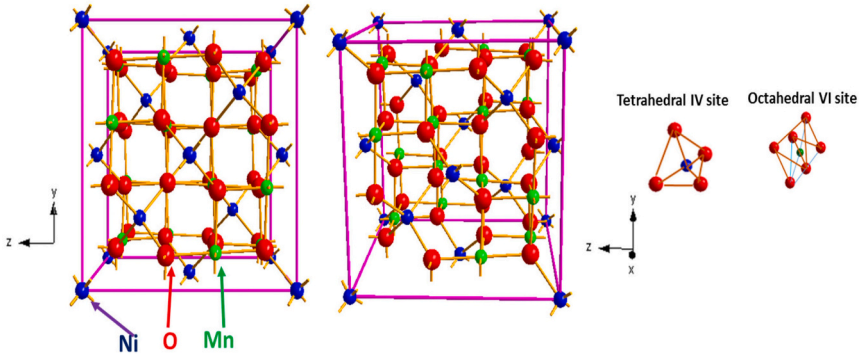

(a)

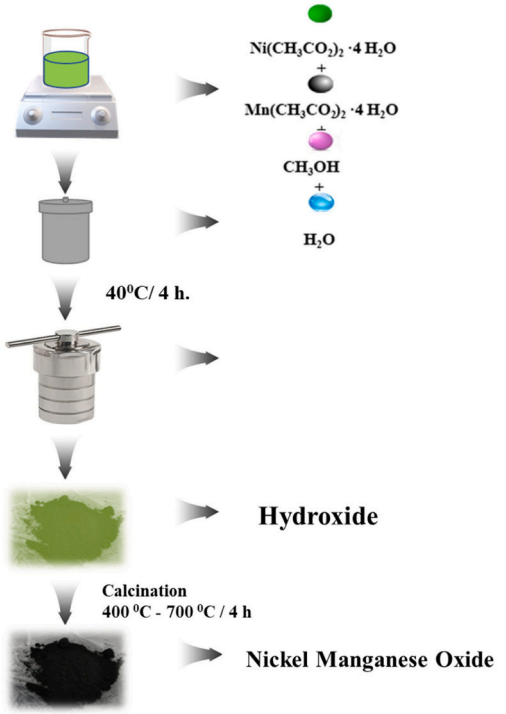

(b)

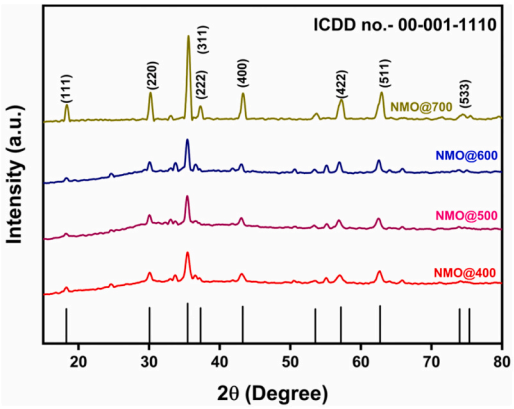

(c)

Fig. 1. (a) Crystallographic structure of $NiMn_2O_4$ NSs 2-D and 3-D synthesized by hydrothermal method. (b) Schematic illustration of synthesis of $NiMn_2O_4$-NSs by hydrothermal method. (c) XRD patterns of the NMO@400, NMO@500, NMO@600, and NMO@700 NSs synthesized by hydrothermal method at calcination temperatures of 400 °C, 500 °C, 600 °C and 700 °C, respectively.

more redox active sites during the redox process. Co-based oxides are hazardous and relatively expensive. As a result, Ni and Mn-based oxides were more advantageous for supercapacitors. Numerous techniques, including morphological modification, the hetero-structures development, and the cross-breeding of conducting materials with increased specific surface area, have been employed for the fabrication of high-performance $NiMn_2O_4$-based electrode materials [18]. $NiMn_2O_4$ can now be produced by sol-gel [19], hydrothermal [20], co-precipitation [21], combustion [22], and spray pyrolysis [23] processes. Among these, hydrothermal processes offer a practicable way for the grounding of mixed metal salts that participates in an impressive amount of mixing, producing NPs with a large surface area and smaller crystallites and good electrical conductivity, which have assisted in monitoring the geomorphology of the quantifiable regions [24]. Fig. 1 displays the cubic phase of prepared $NiMn_2O_4$. The crystalline structure of $NiMn_2O_4$ is 2-D and 3-D, respectively, with Ni occupying the octahedral region and Mn occupying both the octahedral and tetrahedral regions [25].

Wei et al. [26] recently reported that hydrothermally produced sheet-like $NiMn_2O_4$ NPs grown on nickel foam (NF) showed superior electrochemical characteristics with a Cs of 662.5 Fg^{-1} at a current density of 1 Ag^{-1} in a 6 M KOH electrolyte. Supercapacitor electrodes with a Cs of 762 Fg^{-1} at a scan rate of 5 mVs^{-1} in a 6 M KOH electrolyte were synthesized by Dhas et al. using the sol-gel process [27]. By using a computerized spray pyrolysis technique, Chavan et al. were able to create $NiMn_2O_4$ thin films with a Cs of 460 Fg^{-1} at a scan rate of 5 mVs^{-1} in a 2 M KOH electrolyte [28]. To synthesize a series of rGO/$NiMn_2O_4$/PANI nanocomposite electrodes Sahoo et al. used the hydrothermal technique [25].

There is an urgent need for detailed work on $NiMn_2O_4$-based materials in terms of understanding the reasons behind the understanding of fluctuations in the properties of current density and power density and cyclic stability. However, like many other TMOs, $NiMn_2O_4$-based electrodes are still limited by their low-rate capacity with high capacitance [25,27]. Using a hydrothermal process, Bhagwan et al. created a $NiMn_2O_4$ electrode with a Cs of 410 Fg^{-1} at a current density of 1 Ag^{-1}. A solid-state asymmetric supercapacitor based on $NiMn_2O_4$ nanowires as the active material was also reported by this group. It offered a specific energy of 95 $Whkg^{-1}$ and a specific power of 1030 $kWkg^{-1}$ [29]. Asymmetric supercapacitors based on CNT@$NiMn_2O_4$/AC were previously reported by Nan et al. [30]. These devices exhibit outstanding electrochemical performance at a potential window of 0 to 1.7 V and high Cs from 151 to 72.8 Fg^{-1} as the current density increases from 1 to 20 Ag^{-1}.

$NiMn_2O_4$-NSs are made and deposited on NF using a universal and controllable hydrothermal process. In-depth research has been done on the crystalline structure, shape, chemical content, and elemental composition of $NiMn_2O_4$-NSs. NM-NF electrodes have been developed using $NiMn_2O_4$-NSs produced at temperatures of 400, 500, 600, and 700 °C. We discovered that NMO@500-NF exhibits significantly better Cs compared to other electrodes, and we also noticed the synergistic effect of the coexistence of two elements, Ni and Mn, in the $NiMn_2O_4$ host structure. The cycling investigation found that the NMO@500-NF electrode demonstrated long-term chemical stability by retaining 91.2 % of its charge across 10,000 CV cycles. Additionally, symmetric supercapacitor devices (SSCs) based on NM-NSs exhibit high Cs of 72.9 Fg^{-1} at 3 mAg^{-1}, which is comparable to good specific energies of 11 $Whkg^{-1}$ and 857 Wkg^{-1} and capacitance retention of 93.7 % over 5000 cycles.

2. Experimental section

2.1. Materials used in the preparation of $NiMn_2O_4$ NSs

Nickel (II) acetate tetrahydrate [Ni $(CH_3COO)_2{\cdot}4H_2O$], manganese (II) acetate tetrahydrate [Mn $(CH_3COO)_2{\cdot}4H_2O$], methanol (CH_3OH), hydrochloric acid (HCl), NF, carbon black, polyvinylidene fluoride (PVDF), *N*-methyl-2-pyrrolidone (NMP), were purchased from Loba Chemie Pvt. Ltd., Mumbai (India). All AR-grade were used as received without further modifications.

2.2. Synthesis of $NiMn_2O_4$ NSs by hydrothermal method

$NiMn_2O_4$ NSs were synthesized via a facile hydrothermal method and calcination treatment. First, nickel (II) and manganese (II) acetates were taken in a ratio of 1:2 and suspended separately in methanol and double-distilled water (DDW) for 35 min using an ultrasonic process. The manganese acetate solution was transferred into the beaker of nickel acetate solution. After that, ammonia was gradually added to reach a pH of 8 to 9 while being stirred at 400 rpm for an additional 30 min to obtain a homogeneous solution. Then, the resulting mixture was immersed into a 50 mL Teflon-lined autoclave reactor and heated to 110 °C in the air for 5 h to carry out chemical reaction. Afterward, the stainless steel autoclave was allowed to cool naturally at ambient temperature. The resulting product was rinsed five times with ethanol before being calcined for 4 h at 400, 500, 600, and 700 °C. After calcination, the samples are designated as NMO@400, NMO@500, and NMO@600, and NMO@700 respectively. As the calcination temperature increases, the organic component burns out. Along with this, an oxide network is built, and some electrochromic behavior changes are made. Fig. 1(b) shows the scheme for making $NiMn_2O_4$-NSs using a hydrothermal process.

Step-I

$$(CH_3COO)_2Ni + 2(CH_3COO)_2Mn \xrightarrow{6\ CH_3OH} Ni(OH)_2 + 2\ Mn(OH)_2 + 6\ CH_3COOCH_3$$

Nickel Acetate	Manganese Acetate		Nickel Hydroxide	Manganese Hydroxide	Methyl Acetate

Step-II

$$Ni(OH)_2 + 2\ Mn(OH)_2 + 6\ CH_3COOCH_3 \xrightarrow{calcination} NiMn_2O_4 + 7\ CO_2 + 11\ CH_2 + 10\ H_2$$

Nickel Manganese Oxide

2.3. Characterization techniques

The produced $NiMn_2O_4$ NSs were characterized by X-ray diffraction (XRD), field emission scanning electron microscopy (FE-SEM), energy-

Table 1
Crystal structure parameters of the NMO@400, NMO@500, NMO@600 and NMO@700 NSs prepared by the hydrothermal method.

Miller indices (hkl)	Interplanar distance [d_{hkl}] (Å)				Lattice parameters [a = b = c] (Å)				Average crystallite size (nm)			
	NMO@400	NMO@500	NMO@600	NMO@700	NMO@400	NMO@500	NMO@600	NMO@700	NMO@400	NMO@500	NMO@600	NMO@700
(111)	4.89	4.87	4.86	4.875	8.47	8.47	8.42	8.41	10.1	10.9	18	26.6
(220)	2.98	4.97	2.97	2.99	8.45	8.45	8.42	8.41				
(311)	2.53	2.53	2.53	2.53	8.45	8.44	8.40	8.40				
(222)	2.46	2.45	2.45	2.41	8.37	8.37	8.50	8.52				
(400)	2.12	2.11	2.11	2.11	8.44	8.44	8.41	8.41				
(422)	1.61	2.6	1.59	1.61	8.44	8.44	7.93	7.93				
(511)	1.58	1.57	1.55	1.54	8.052	8.05	7.71	7.71				
(440)	1.49	1.49	1.48	1.48	8.44	8.47	8.43	8.42				

dispersive X-ray spectroscopy (EDX), X-ray photoelectron spectroscopy (XPS), Brunauer Emmett Teller (BET), etc. On a Bruker AXS, (Diffractometer D2, Germany) diffractometer, XRD analysis was carried out spanning the wavelength range of 2θ from 15° to 80° using a Cu-K_α radiation source. The morphology of the $NiMn_2O_4$ NSs was examined by FE-SEM (JSM-6160, Japan). By using XPS analysis on a ULVAC-PHI Quantera SXM (Japan), the oxidation states and component elements found in the $NiMn_2O_4$- NSs were assessed. To determine the chemical composition, EDX (X-act-Oxford Instruments, Japan) spectroscopy was employed. Utilizing N_2 adsorption-desorption isotherms; the Brunauer-Emmett-Teller (BET) technique was opted to measure the surface area of $NiMn_2O_4$ NSs. (Model-NOVA 1000e Quanta chrome, Japan).

3. Result and discussion

3.1. X-ray diffraction (XRD)

The $NiMn_2O_4$ NSs produced by the hydrothermal approach are depicted in Fig. 1(c) in an X-ray diffraction (XRD) plot after being further annealed at 400 °C, 500 °C, 600 °C, and 700 °C. These temperatures are designated as NMO@400, NMO@500, NMO@600, and NMO@700, respectively. It can be observed that all NMs' XRD patterns peak at the following reflection planes: (111), (220), (311), (222), (400) (422) (511) (533) and (622). Thus, it is confirmed that a single phase with a cubic spinel structure formed. All NMO-NSs reflection peaks are compared to the $NiMn_2O_4$ ICDD card No. 00-001-1110 and confirmed to be totally compatible with typical reflection peaks.

Eqs. (1) and (2) are used to determine the lattice constants a, b, and c, as well as the inter-planar separation (d_{hkl}).

$$a = d_{hkl}\sqrt{h^2 + k^2 + l^2} \tag{1}$$

$$d_{hkl} = \frac{n\lambda}{2\,sin(\theta)} \tag{2}$$

Where dhkl is the interplanar distance, (hkl) are the Miller indices, λ is the wavelength of X-ray used and θ is Bragg's angle of reflection.

It is found that as the annealing temperature is increases, the reflection peaks get sharpen and that the crystallinity is improves. The crystallite size of NM-NSs is calculated using the Scherrer formula [31–32]:

$$D = \frac{0.9\,\lambda}{\beta cos\theta} \tag{3}$$

Where D is crystallite size (nm), 0.9 is a dimensionless shape factor, λ is the X-ray wavelength (nm), β is the full width at half maximum (rad), and θ is the diffraction angle (rad). The fundamental crystal structural parameters for $NiMn_2O_4$-NSs are from XRD patterns and are described in Table 1. It has been discovered that the nanocrystalline sizes of NM-NSs grow with calcination temperature, from 10.1 nm at 400 °C to 26.6 nm at 700 °C.

3.2. XPS analysis

To determine the chemical composition and oxidation states of the various elements in the hydrothermally synthesized NMO@500-NSs, XPS analysis was performed. The typical XPS survey spectrum is shown in Fig. 2, and it confirms the existence of the elements Ni 2p, Mn 2p, O1s, and C1s in the NMO@500-NSs electrode without any other impurities. The accidental carbon contamination brought on by the NMO@500-NSs being exposed to the atmosphere is thought to be the reason for the C component's presence. The Ni 2p spectrum can be seen in Fig. 2(b), and it is composed of two spin-orbit doublets that are typical of Ni $2P_{1/2}$ and Ni $2P_{3/2}$, which are separated by two shakeup satellite peaks. The Gaussian peak fitted at binding energies at 872.5 eV is ascribed to Ni $2P_{1/2}$, while Ni 2P3/2 is responsible for the peak fitted at

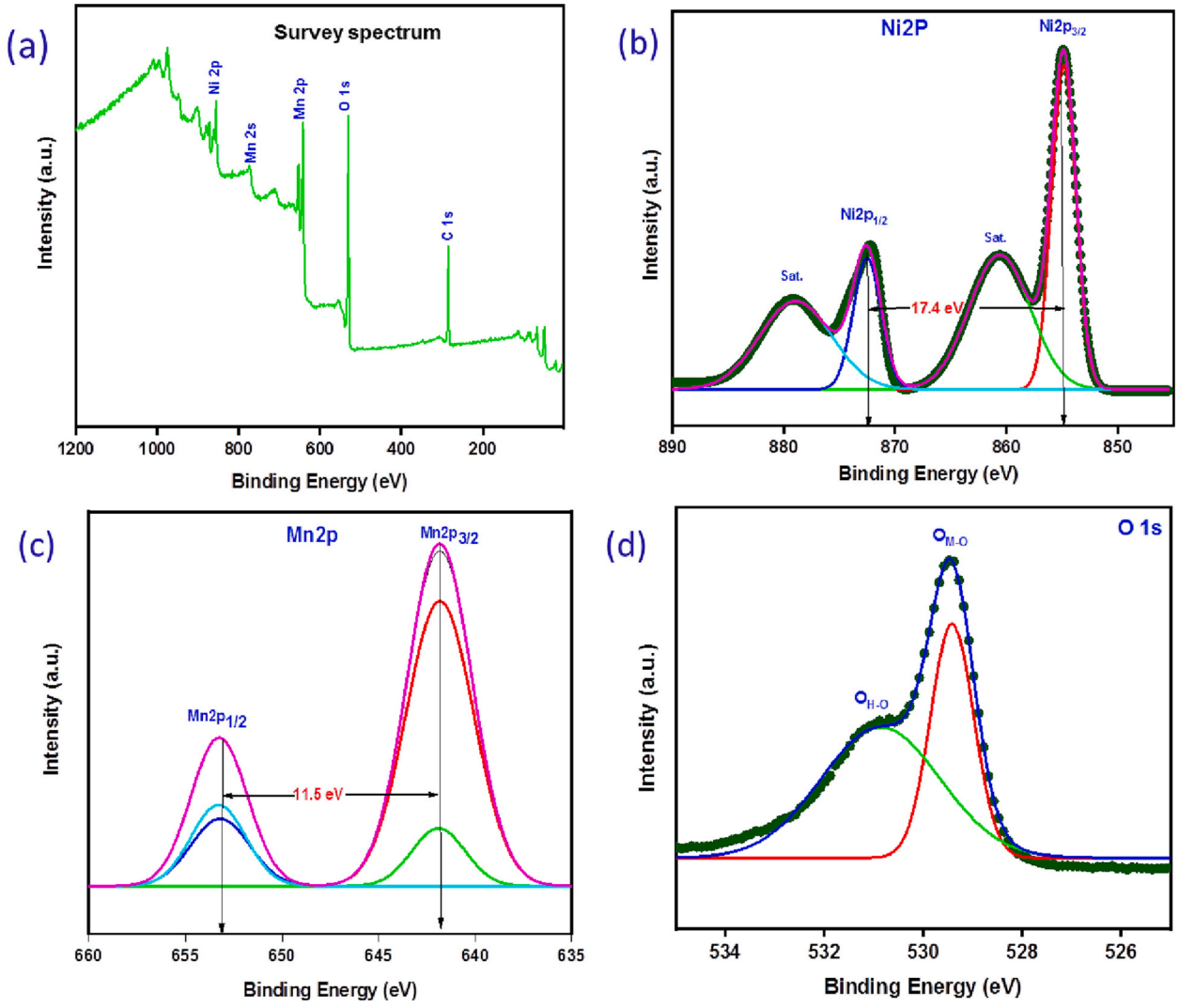

Fig. 2. (a) XPS survey scan spectrum of the NMO@500-NSs synthesized by hydrothermal method, XPS narrow scan spectrum of (b) Ni 2p (c) Mn 2p (d) O 1s.

854.6 eV. Similar to this, the Mn 2p spectra depicted in Fig. 2(c) is made up of two spin-orbit doublets that are typical of Mn $2P_{1/2}$ and Mn $2P_{3/2}$, and their respective binding energies are 853.2 eV and 641.8 eV. For O 1s, two prominent humps were seen at 530.7 eV and 529.5 eV as shown in Fig. 2(d), which, respectively, relate to the O—H species of the surface adsorbed water molecules, oxygen ions in low surface coordination, and the type of metal-oxygen interactions [33]. These findings support the results found in the literature for spinel-$NiMn_2O_4$ [34] that the surface of the NMO@500- NSs as prepared by hydrothermal technique has a composition of Ni^{2+}, Ni^{3+}, Mn^{2+}, Mn^{3+}, and O_2. The Ni 2p, Mn 2p, and O 1s Gaussian fitted XPS spectra with high resolution identify the improved material's electrochemically promising valence states.

3.3. Morphologies study

Fig. 3(a–d) illustrates the FE-SEM micrographs of hydrothermally produced NMO-NSs at magnifications of 25,000 X and various calcination temperatures. As the calcination temperature is raised, morphological changes were observed in samples calcined at various temperatures. FE-SEM micrographs show a noticeable increase in particle size as the calcination temperature rises. It is noted that the NM-NSs formed at 400 °C have a smooth shape. The insertion of ions has increased due to the creation of pores and nanoparticles in the NM-NSs made at 500 °C. Additionally, many pores have been discovered on the surfaces of NMO@500-NSs, and their presence facilitates the intercalation and deintercalation of electrolyte ions. Significant nanoplate growth can be seen in samples annealed at 600 °C and 700 °C. The length of the ion diffusion path will be prolonged by the large size of NSs, resulting in inferior rate performance.

3.4. EDX analysis

The elemental composition of the NM-NSs has been assessed by EDX analysis to determine their purity. The EDX spectrum of the NMO-NSs synthesized at various calcination temperatures is shown in Fig. 3 (e–h), which verified the existence of Ni, Mn, and O elements. Tables with their atomic percentages are provided inset within the matching EDX spectrum. It is evident that the constituent element's stoichiometric ratio in NMO@500-NSs appears to be almost stoichiometric.

3.5. BET analysis

The N_2 adsorption-desorption isotherms, shown in Fig. 4 are used to calculate the BET specific surface areas of the NM-NSs as prepared by the hydrothermal approach with varied calcination temperatures

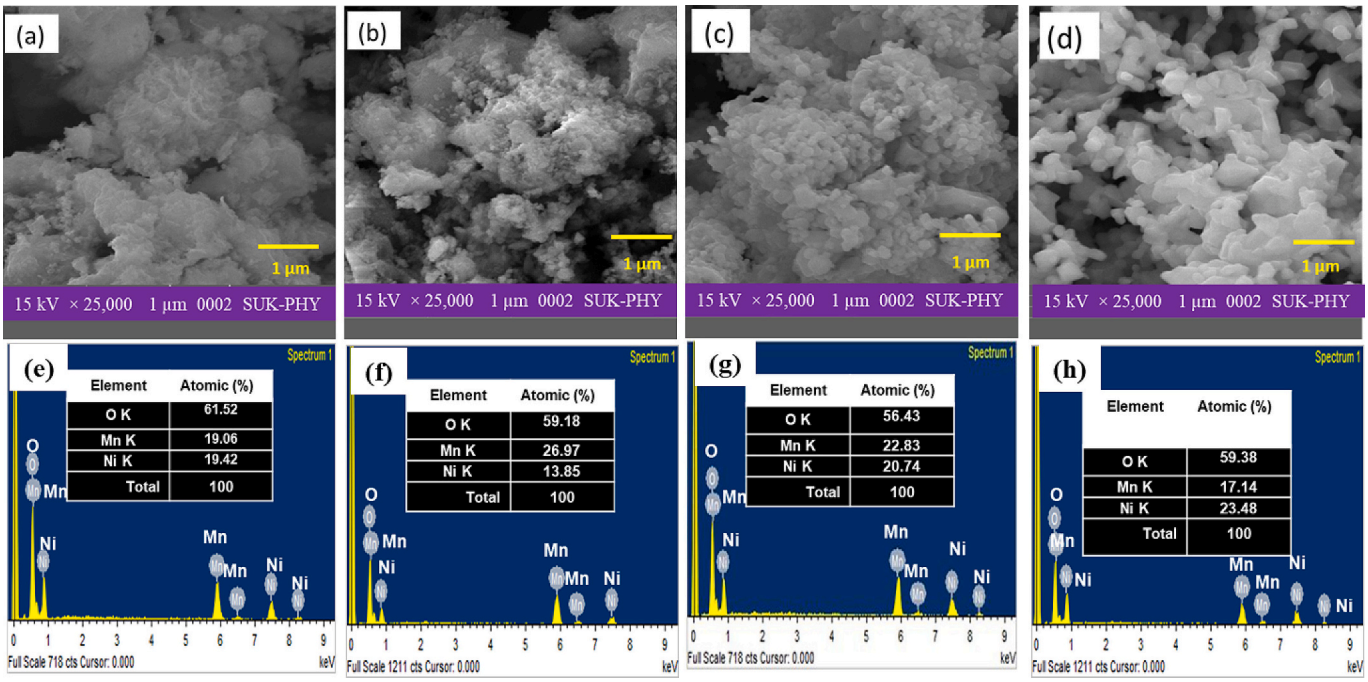

Fig. 3. FE-SEM micrographs of the NM-NSs at the magnification of × 25,000 (a) NMO@400 (b) NMO@500 (c) NMO@600 and (d) NMO@700 NSs synthesized by hydrothermal method. EDX spectra of the (e) NMO@400 (f) NMO@500 (g) NMO@600 and (h) NMO@700 NSs synthesized by hydrothermal method.

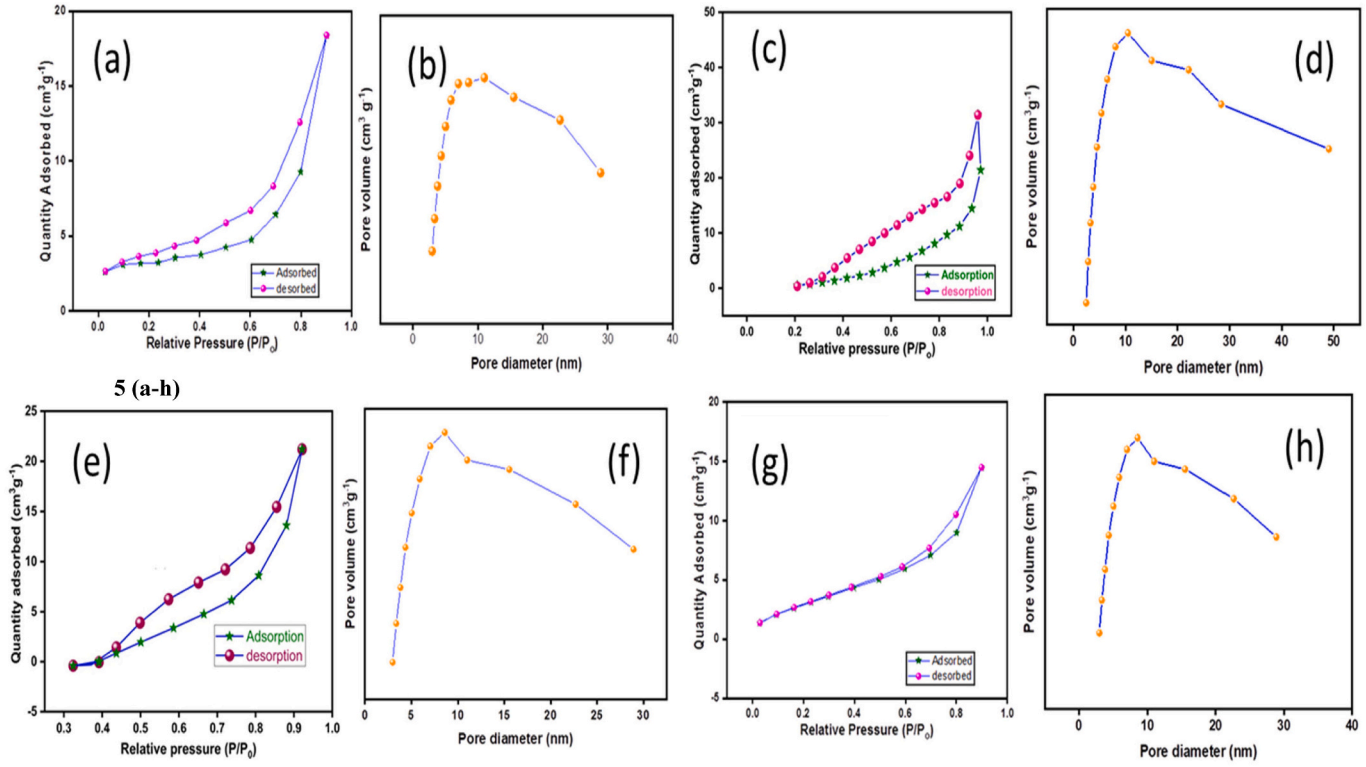

Fig. 4. Nitrogen adsorption-desorption isotherms of the (a) NMO@400, (c) NMO@500 (e) NMO@600 and (g) NMO@700 NSs. BJH curve of the (b) NMO@400, (d) NMO@500 (f) NMO@600 and (h) NMO@700 NSs.

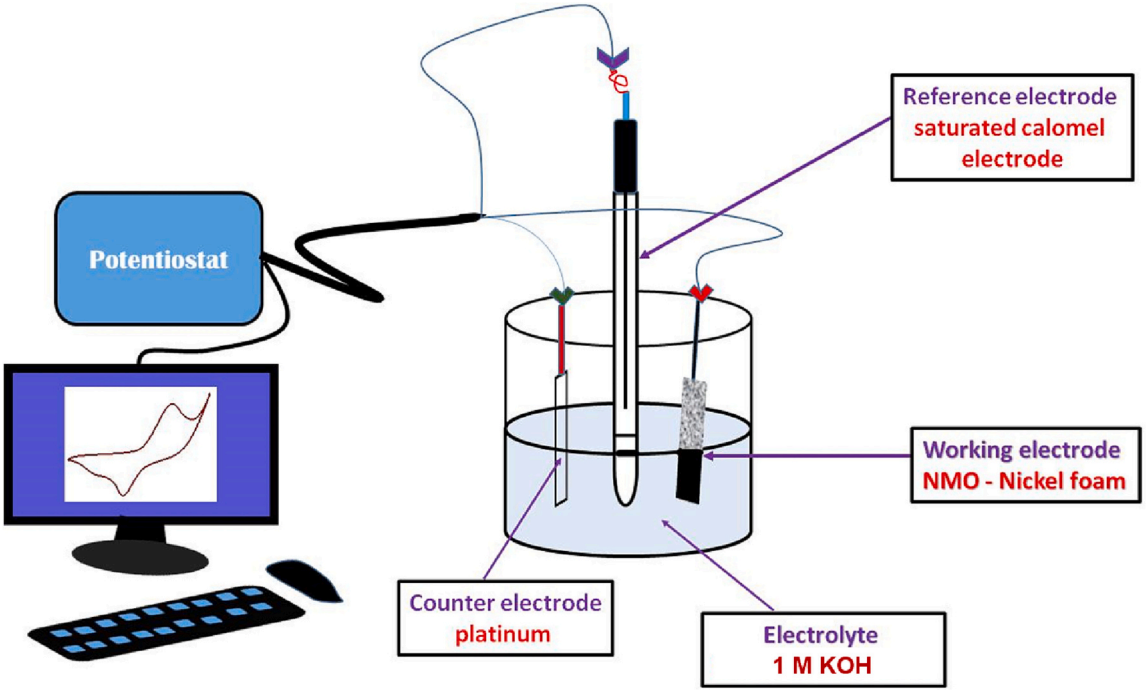

Fig. 5. Schematic of the three-electrode measurement setup for the studying electrochemical properties.

(NMO@400, NMO@500, NMO@600, and NMO@700) (a,c,e,g). As shown in Fig. 4, the relevant pore size distributions are evaluated using Barrett-Joyner-Halenda (BJH) (b,d,f,h). The computed BET specific surface areas of the NMO@400, NMO@500, NMO@600, and NMO@700 are 41.34 m^2g^{-1}, 58.22 m^2g^{-1}, 33.12 m^2g^{-1}, and 18.84 m^2g^{-1}, respectively. All the NM-NSs show a hysteresis loop. The average pore sizes of the NMO@400, NMO@500, NMO@600, and NMO@700 NSs are 6.3 nm, 3.1 nm, 11.7 nm, and 22.3 nm, respectively, and the predicted pore volumes are 0.19 cm^3g^{-1}, 0.23 cm^3g^{-1}, 0.16 cm^3g^{-1}, and 0.12 cm^3g^{-1}. These pore size distributions are shown in Fig. 4(b,d,f,h). In addition to offering size and shape selectivity and high surface areas, these materials have large interfacial areas and pore volumes, which lower the material's transport constraints and make it easier for ions to reach the active sites. High surface area mesoporous materials are thought to improve electrochemical performance. Mesoporous materials also have improved surface areas due to their pores, which also allow for the storage of ions [34]. NMO@500 NSs have a big pore volume, a low average pore size, and a high surface area when compared to NMO@400, NMO@600, and NMO@700 NSs. These NMO@500-NSs characteristics are more advantageous for electrolyte ion diffusion and transport during the intercalation-deintercalation process in supercapacitors.

3.6. Preparation of working electrode

At first, NF (thickness: 1.6 mm) was ultrasonically treated with ethanol, 4 M hydrochloric acid, and double-distilled water for 30 min. to remove the oxide layer and other impurities [35]. The working electrodes were prepared using 75 % active electrode material (NMO-NSs), 15 % activated carbon, and 10 % polyvinylidene fluoride binder in *N*-methyl-2-pyrrolidinone prior to electrochemical measurements. To produce a uniform slurry, the mixture was sonicated for half an hour. After that, the produced slurry was applied to 1 cm^2 of previously cleaned nickel foam and heated for 4 h at 110 °C. About 6 mg of the active substance is coated on NF. The electrochemical testing has been done using electrodes made from NMO@400, NMO@500, NMO@600, and NMO@700 NSs. The saturated calomel electrode (SCE) is used as a reference electrode to assess the electrochemical characteristics of the NM-NF electrodes in the conventional three-electrode system. The working electrode is NMO-NF, the counter electrode is platinum, and the electrolyte is 1 M KOH. The schematic representation of a three-electrode setup at room temperature is shown in Fig. 5 in order to evaluate the electrochemical performance of the as-synthesized NMO-NF.

3.7. Electrochemical performance of the NM-NF electrode

The electrochemical properties of $NiMn_2O_4$-NSs as an electrode material for an electrochemical capacitor are examined (EIS) using cyclic voltammetry (CV), galvanostatic charge/discharge (GCD), and electrochemical impedance spectroscopy. The cyclic voltammograms for NMO@400-NF, NMO@500-NF, NMO@600 -NF, and NMO@700 -NF are shown in Fig. 6(a–d) at scan rates of 5 mVs^{-1}, 10 mVs^{-1}, 20 mVs^{-1}, 50 mVs^{-1}, 80 mVs^{-1}, and 100 mVs^{-1}, respectively. Although the present density magnitude and potential range are different, the CV plots demonstrate a similar pattern. Two strong peaks are seen, which correlate to the typical pseudo-capacitance behavior and are caused by Faradaic redox processes within the system. The oxidation peak was produced by the transformation of $NiMn_2O_4$ to NiOOH and MnOOH, whereas the reduction peak was produced by the opposite reaction. The redox mechanism outlined in the following equations (Eqs. (4) and (5)) is what causes the charge storage in the NM-NF electrode.

$$NiMn_2O_4 + OH^- + H_2O \leftrightarrow NiOOH + 2MnOOH + e^- \quad (4)$$

$$MnOOH + OH^- \leftrightarrow MnO_2 + H_2O + e^- \quad (5)$$

The boost in current density is caused by the CV plot of NM-NF electrodes at calcination temperatures of up to 500 °C. Thus, as the

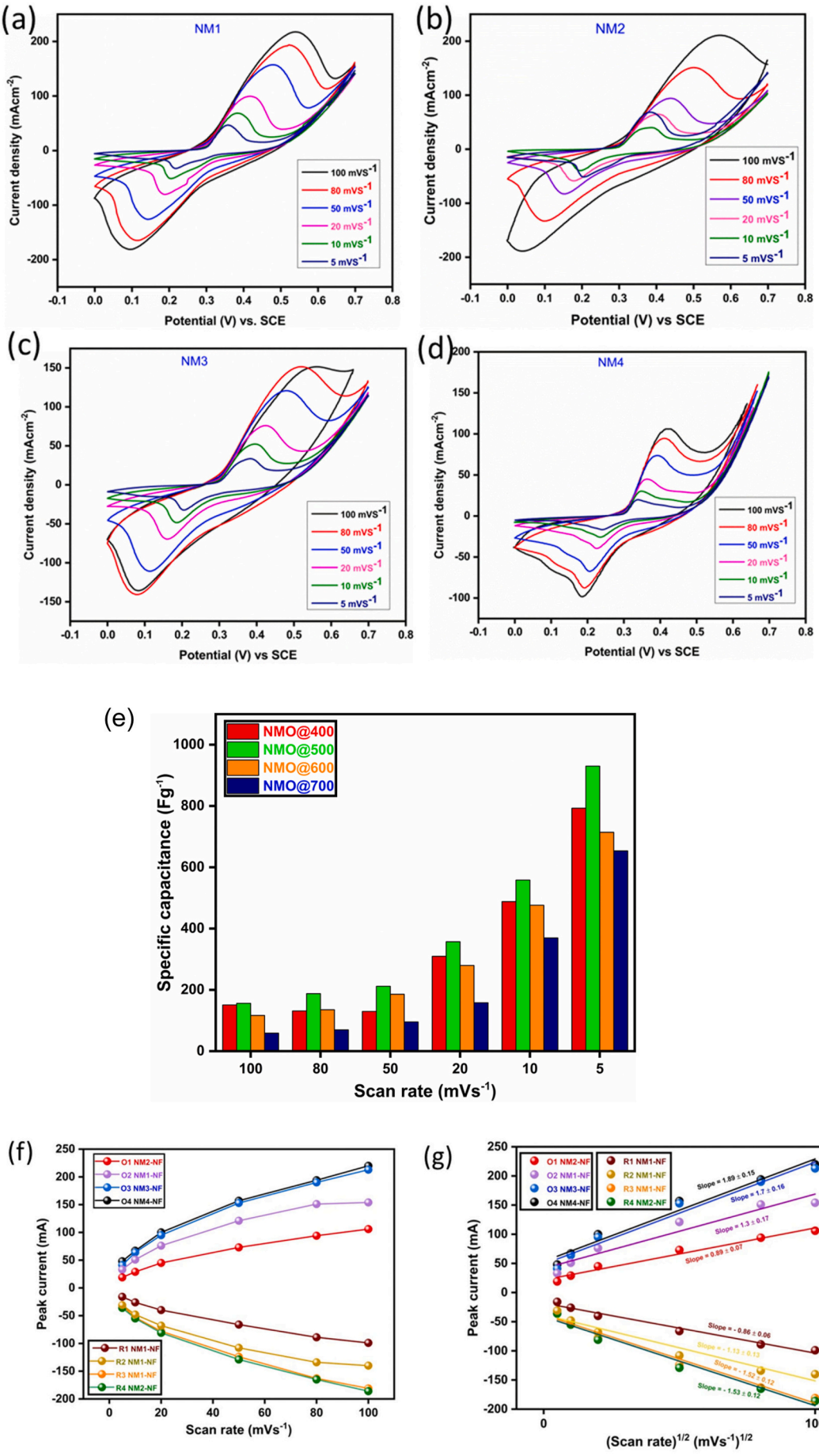

(caption on next page)

Fig. 6. CV plots of the (a) NMO@400-NF (b) NMO@500-NF (c) NMO@600-NF (d) NMO@700-NF electrodes at the various scan rates in 1 M KOH electrolyte (e) Plot of specific capacitance vs. scan rates of the NMO@400-NF, NMO@500-NF, NMO@600-NF and NMO@700-NF electrodes in 1 M KOH electrolyte. Plot of redox peak currents for NMO@400-NF, NMO@500-NF, NMO@600-NF and NMO@700-NF (f) vs scan rate and (g) vs square root of scan rate.

calcination temperature increases from 400 °C to 700 °C, current density decreases. The intercalation de-intercalation of OH^- ions in the $NiMn_2O_4$ matrix charge transfer affects the rate capabilities. Many electrode materials can be utilized because, at a slow sweep rate, the charges in the electrolyte have enough time to undergo surface redox reactions. At high scan rates, however, all active sites are not accessible to the electrolyte ions due to a lack of time, leading to subpar performance. Using the CV curves, Eq. (6) was employed to determine the Cs of the NM-NF electrodes [36].

$$Cs = \frac{1}{mv(V_f - V_i)} \int_{V_i}^{V_f} I\,(V)dv \tag{6}$$

The working potential window is (V_f-V_i) and the specific capacitance of the NM-NF electrode is (Fg^{-1}), m (effective mass of the active electrode material is (g)), I (current density is (mAg^{-1})), V (scan rate is (mVs^{-1})), and Cs (specific capacitance). When the scan rate is decreased from 100 mVs^{-1} to 5 mVs^{-1}, the Cs of NMO@500-NF rise in proportion by a factor of five. The low value of 714 Fg^{-1} produced by NMO@600 -NF is another factor. NMO@700 -NF has a low specific capacitance of 654 Fg^{-1} compared to the other two electrode materials. Both NMO@500-NF and NMO@400-NF have Cs values of 930 Fg^{-1} and 793 Fg^{-1}. The development of the NMO@500-NF electrode supports all hypotheses and interpretations drawn from the various characterization techniques, as well as the material's high porosity, high specific surface area, and the presence of numerous types of pores. Additionally, as demonstrated in the plot of Cs vs. scan rate in Fig. 6(e), the Cs value rises as the scan rate falls. This information shows that the specific capacitance of NMO@500-NF and NMO@400-NF is greater than that of other capable electrode materials. The oxidation and reduction peak currents measured for the NMO@400-NF, NMO@500-NF, NMO@600-NF, and NMO@700-NF electrodes are displayed against the scan rate as well as the square root of that rate in Fig. 6(f–g). The peak currents have a nonlinear relationship with sweep rate, as shown in Fig. 6(f), whereas they have a nearly linear relationship with the square root of scan rate, as shown in Fig. 6(g). This indicates that the redox reaction is diffusing driven in this case, as indicated by the Randles-Sevcik equation, as stated below [38].

$$I_p = \left(2.687 \times 10^5\right) n^{3/2}\, V^{1/2}\, D^{1/2}\, A\, C_0 \tag{7}$$

where Ip stands for peak current, n for the number of electrons transported in the electrochemical method (n = 2), V for sweep rate, C_0 for KOH concentration, A for geometrical electrode area and D for diffusivity of the material. As the materials' diffusivity increases, an electrolyte's specific capacitance rises. As a result, the diffusivity may be determined from the slope of the line. Thus, in the KOH electrolyte, the diffusivity of the active materials is as follows: NMO@500-NF > NMO@400-NF > NMO@600-NF > NMO@700-NF.

In order to evaluate the quantitative electrochemical characteristics of the NM-NF electrode, GCD analysis was performed. The GCD curves of the NMO@400-NF, NMO@50-NF, NMO@600-NF, and NMO@700-NF electrodes are shown in Fig. 7(a–d) for various current densities of 3 $mAcm^{-2}$, 4 $mAcm^{-2}$, and 5 $mAcm^{-2}$. The discharge time for the NMO@500-NF electrode is the longest at 3 $mAcm^{-2}$ current density and gets shorter as the annealing temperature increases. The charging time increases while the discharge time decreases when comparing the NMO@500-NF electrode to the NMO@400-NF, NMO@600-NF, and NMO@700-NF electrodes. The Cs of the NM-NF electrodes are calculated using the GCD curves and Eq. (8) [37].

$$Cs = \frac{I\Delta t}{m(V_f - V_i)} \tag{8}$$

Where Cs is the specific capacitance (Cs) of the NM-NF electrode (Fg^{-1}), m is the mass of the active electrode material (g), respectively and (V_f–V_i) is the working potential window.

According to Fig. 7(e), there is a correlation between Cs and current densities used for charging and discharging. The result indicate that the "optimal" electrode, with good CS values, is NMO@500-NF. Table 2 provides an overview of how the CS is calculated for NM-NF electrodes using CV plots at various scan rates and CD plots at various current densities in 1 M KOH electrolyte. The formulas below are used to calculate the highest specific energy (Esp), specific power (Psp), and Coulombic efficiency (η) from the GCD for the NMO@500-NF electrode, respectively [27].

$$E_{sp} = \frac{0.5 \times C_s \times V^2}{3.6} \tag{9}$$

$$P_{sp} = \frac{3600 \times E_{sp}}{T_d} \tag{10}$$

$$\eta = \frac{T_d}{T_c} \times 100 \tag{11}$$

where C_s is the specific capacitance, T_d is the discharge time, T_c is the charging time and V is the scan rate. The calculated values of E_{sp}, P_{sp}, and η of the NMO@500-NF electrode in a 1 M KOH electrolyte is 24 $Whkg^{-1}$, 233 Wkg^{-1}, and 99.2 %, at 3 $mAcm^{-2}$ respectively.

As seen in Fig. 7(f), the EIS is a tool used to assess the circuits and associated resistance between the electrolyte and electrode. A sine wave with 6 mV amplitude and a frequency range of 1 Hz to 100 kHz was supplied in a 1 M KOH aqueous solution. The electrochemical capacitor's overall impedance is caused by ionic and electronic processes. Ionic diffusion, which occurs when electrolyte charges move through pores, is what causes ionic resistance. Charge transfer resistance (Rct), a factor in Faradaic processes, is what gives the appearance of a semi-circle in the high-frequency zone. The Rct increases as the semicircle's size decreases, indicating a higher Cs. We observed Rct values of 6.8 Ω, 6.2 Ω, 7.4 Ω, and 7.9 Ω for NMO@400-NF, NMO@500-NF, NMO@600-NF, and NMO@700-NF, respectively. Additionally, it was found that NMO@400-NF, NMO@500-NF, NMO@600-NF, and NMO@700-NF had Rs values of 0.42 Ω, 0.38 Ω, 0.49 Ω, and 0.52 Ω, respectively. NMO@500-NF has lower Rct and Rs values than the other electrodes. The NMO@500-NF electrode has a high conductivity, according to this result. It is linear in the low-frequency range. Additionally, the Warburg impedance (W), which corresponds to charge transfer into the electrodes in bulk through the pores, is shown by the inclination lines in the lower frequency region. The vertical slope shows increased capacitance performance in the low-frequency range. Because of its linearity, the NMO@500 NF electrode is reliable as a superior and ultimate capacitor. The space between the two zones is called the "knee frequency" region.

Electrochemical CV studies were carried out in 1 M KOH electrolyte to learn as much as possible about the cyclic stability of the NMO@500-NF electrode. By analyzing the fluctuations in Cs as a function of

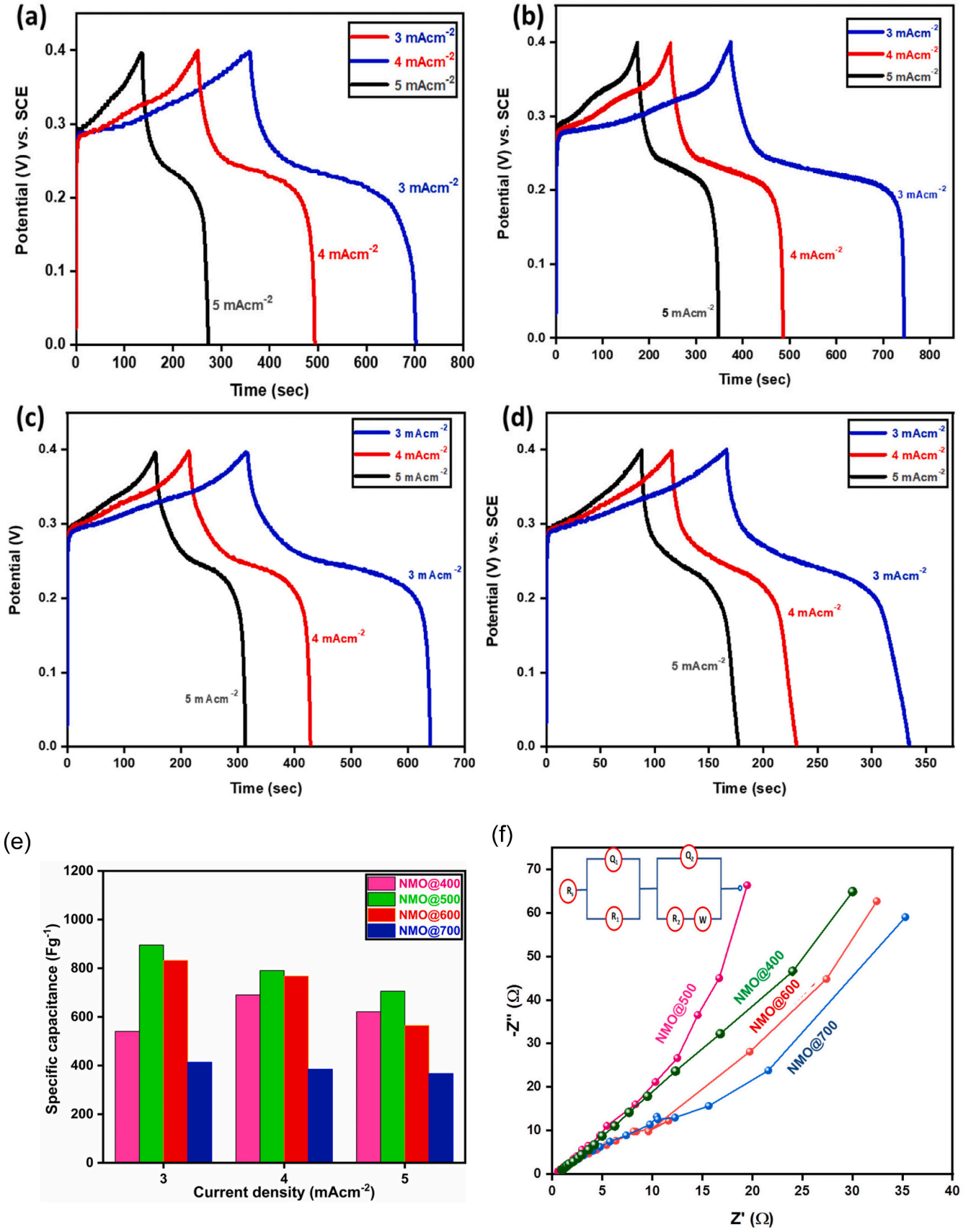

Fig. 7. Comparative GCD plots of the (a) NMO@400-NF (b) NMO@500-NF (c) NMO@600-NF (d) NMO@700-NF electrodes at the various current densities in 1 M KOH electrolyte. (e) Plot of specific capacitance vs. current densities of the NMO@400-NF, NMO@500-NF, NMO@600-NF and NMO@700-NF electrodes in 1 M KOH electrolyte (f) Nyquist plot of the NMO@400-NF, NMO@500-NF, NMO@600-NF and NMO@700-NF electrodes in 1 M KOH electrolyte. (g) Plot of capacitance retention rate of the NMO@500-NF electrode vs. cycle number in 1 M KOH electrolyte.

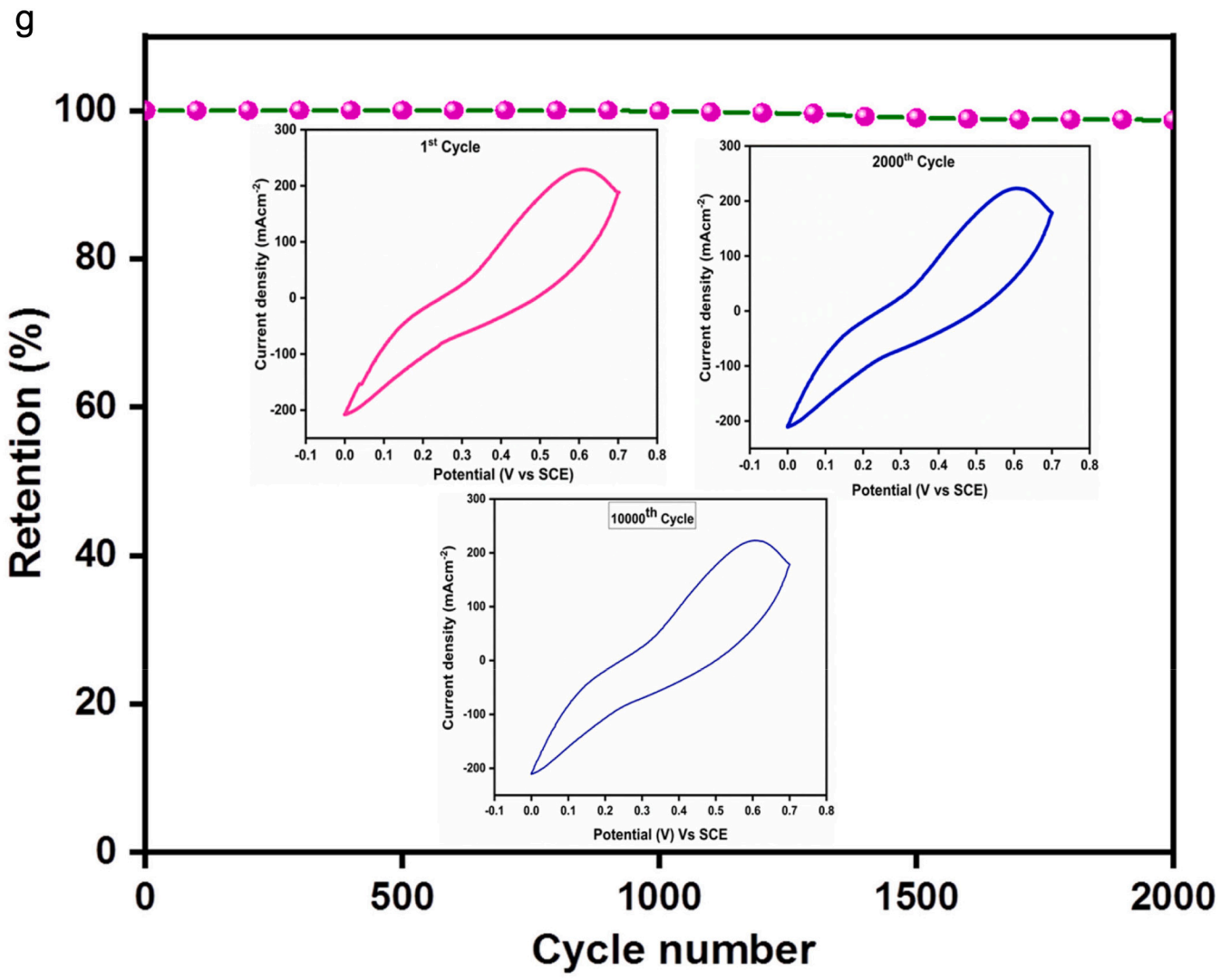

Fig. 7. (*continued*).

charging-discharging cycles at a scan rate of 100 mVs^{-1}, as shown in Fig. 7(g), the stability of the NMO@500-NF electrode was thoroughly investigated. The NMO@500-NF electrode maintained 91.2 % of its initial capacitance across 10,000 cycles, demonstrating the electrode's extraordinary durability as a capacitor.

Table 3 illustrates the comparison of the calculated Cs, the obtained morphological structure, the current collector used, the electrolyte used, the synthesis method used, and the capacitance retention after the number of cycles of the $NiMn_2O_4$-based electrode material with other research groups.

3.8. Assembly of the symmetric supercapacitor device (SSCs)

Two NMO@500-NF based electrodes are joined together to form the SSCs. Fig. 8(a) displays the schematic for NMO@500-NF based SSCs together with real photos of both electrodes. In order to create the polyvinyl alcohol and potassium hydroxide (PVA + KOH) quasi-solid state gel electrolyte, 6 g of PVA precursor, 6 g of KOH, and 60 mL of DDW must be combined. At 90 °C, the mixture must be vigorously stirred until homogenous and viscous. By coating the resultant NMO@500 slurry over nickel foam (2×2 cm^2) and drying it for 6 h in a vacuum furnace at 70 °C, electrodes are fabricated. A bulk loading of approximately 10 mg cm^{-2} of active material was present in each electrode. The clear and viscous solution has been employed as both a separator and a quasi-solid phase electrolyte in the development of NMO@500-NF/NMO@500-NF symmetrical systems. And finally, a VMP3-based biologic potentiostat was used to test a symmetric device.

3.9. Electrochemical performance of SSCs

As shown in Fig. 8(b), the CV plots of the SSCs measured at various sweep rates reveal the redox reaction of Ni^{2+}/Ni^{3+} and Mn^{2+}/Mn^{3+}. The gadget is pseudocapacitive, and the fast faradaic responses over its electrode surfaces demonstrate this. Their interior areas rise as the scan rate rises. The inset of Fig. 8(b) shows the device's real image at the time of measurement. To study the electrochemical characteristics of the SSCs, GCD has been carried out at various current densities. The findings are shown in Fig. 8(c). The Cs of SSCs is calculated using formula 12 [38].

$$Cs = \frac{I}{dv/dt}\left(\frac{1}{m1}+\frac{1}{m2}\right) \quad (12)$$

Table 2
Summarized data of the calculated specific capacitance of the NMO-NF electrodes using CV plots and GCD plots in aqueous 1 M KOH electrolyte.

Scan rates (mVs^{-1})	Specific capacitance of the NM-NF electrode using 1 M aqueous KOH electrolyte from the CV curve				Current density ($mAcm^{-2}$)	Specific capacitance of the NM-NF electrode using 1 M aqueous KOH electrolyte from the CD curve			
	NMO@400	NMO@500	NMO@600	NMO@700		NMO@400	NMO@500	NMO@600	NMO@700
5	793	930	714	654	3	690	895	832	414
10	488	558	476	370	4	621	790	768	385
20	310	357	280	158	5	541	706	565	367
50	129	212	186	95					
80	131	188	135	70					
100	150	156	117	59					

Table 3
Comparison of specific capacitance of the NMO based electrode material from the present research work with other research groups in accordance with, the synthesis method used for preparation of NMO, the morphology used, the electrolyte used, current collector utilized, and % retention of specific capacitance after number of cycles.

Sr. no.	Material	Method of preparation	Morphology	Current collector	Electrolyte	Specific capacitance Cs ($F\ g^{-1}$)	Retention %/after cycles	Ref.
1	$NiMn_2O_4$	Sol-gel	Spherical	Ni-foam	1 M NaOH	658	96.4/1000	[19]
2	$NiMn_2O_4$	Hydrothermal	Nanosheet	Ni-foam	2 M KOH	470.7	89.6/5000	[20]
3	$NiMn_2O_4$/rGO	Co-precipitation method	Nanorods	Ni-foil	1 M Na_2SO_4	693.00	91.38/2000	[21]
4	FeVO4 || $NiMn_2O_4$	Combustion	Polyhedral shape	Stainless steel plate	1 M Na_2SO_4	202	91/15000	[22]
5	$NiMn_2O_4$	Hydrothermal method and post-annealing	Wall-like structure	Ni-foam	1 M Na_2SO_4	177.2 mF/cm^2	89/5000	[24]
6	$NiMn_2O_4$	Hydrothermal method	Nanorod-like	Ni-foam	6 M KOH	662.5	96/1000	[26]
7	$NiMn_2O_4$	Sol-gel	Spherical	Ni-foam	6 M KOH	571	96/2000	[27]
8	$NiMn_2O_4$/rGO	Sol-gel	Spherical-like	Ni-foam	3.5 M KOH	710	91/10000	[39]
9	$NiMn_2O_4$	Sol-gel	–	Ni-mesh	1 M Na_2SO_4	243	96/5000	[40]
10	$NiMn_2O_4$	Sol-gel	Fabric shape	Ni-foam	1 M KOH	303	–	[41]
11	$NiMn_2O_4$	Sol-gel	Spherical	Teflon coated graphite rod	1 M Na_2SO_4	875	91/10,000	[42]
12	$NiMn_2O_4$	Sol-gel	Thin flakes	Ni-foam	1 M KOH	303	5000	[43]
13	$NiMn_2O_4$	Microwave-assisted hydrothermal process	Microspheres	Ni-foam	6 M KOH	768.9	85.8/6000	[44]
14	$NiMn_2O_4$	Hydrothermal	–	Glassy carbon disk	1 M KOH	–	–	[45]
15	$NiMn_2O_4$	Hydrothermal	–	Ni-foil	6 M KOH	151	96.3/5000	[30]
16	$NiMn_2O_4$	Co-precipitation	–	Stainless steel wire mesh.	1 M $LiNO_3$	184	–	[46]
17	$NiMn_2O_4$	Calcinations of oxalate precursors	Bipyramidal	–	–	180	67/1000	[47]
18	$NiMn_2O_4$	Electro spinning	Nano fibers	Graphite sheet	1 M KCl.	170 (±5)	–	[29]
19	$NiMn_2O_4$	Hydrothermal	Nanoplates	Ni-foam	1 M KOH	930	96/2000	This Work

where m_1 and m_2 are the masses of the first and second electrode material, respectively. I, refer to the applied current (mA) and dV/dt is the slope of the discharge curve.

The Cs increased around 1.5 times (from 48 Fg^{-1} to 72.9 Fg^{-1}) when the current density was decreased from 3 to 1 $mAcm^{-2}$, suggesting good electrochemical qualities like Columbic efficiency and super capacitive reversibility at high current density. The specific energy and specific power of the NM-NF/NM-NF SSCs at various current densities are determined using Eqs. (9) and (10) respectively. The SSCs' Cs versus current density is plotted in Fig. 8(d). Fig. 8(e) displays the Ragone curve for the NM-NF/NM-NF SSCs' specific energy and power. The NM-NF/NM-NF SSCs' specific energy reaches 11 $Whkg^{-1}$ at a specific power of 857 Wkg^{-1}; at a power density of 1299 Wkg^{-1}, it then sustains at 8 $Whkg^{-1}$. The cycle stability of the NM-NF/NM-NF SSCs at a current density of 3 $mAcm^{-2}$ is shown in Fig. 8(f). 93 % of the initial Cs is still present after 5000 electrochemical CV cycles, demonstrating good chemical stability. At open circuit potential, the EIS of the symmetric NM-NF/NM-NF capacitor was measured, and the Nyquist curve is shown in Fig. 8(g). The charge-transfer resistance for SSCs was determined to be 9.8 Ω. The Warburg resistance is often known as the slope of the 45° portions of the curve, results from the frequency dependence of charge diffusion in the electrolyte to the electrode surface.

4. Conclusions

In conclusion, a simple hydrothermal technique was used to successfully produce and deposit $NiMn_2O_4$ NSs on Ni foam. The optimized NMO@500-NF electrode has a large specific capacitance, great rate capability, and strong chemical stability Additionally, the combined NMO@500-NF/NMO@500-NF SSCs with a potential range of 0–0.7 V may offer a specific capacitance of 72.9 Fg^{-1} at a current density of 1 mAg^{-1}. A specific energy of 11 $Whkg^{-1}$ was achieved at a specific power of 857 Wkg^{-1}. Therefore, the NMO@500-NF/NMO@500-NF SSCs are promising for electrochemical capacitors.

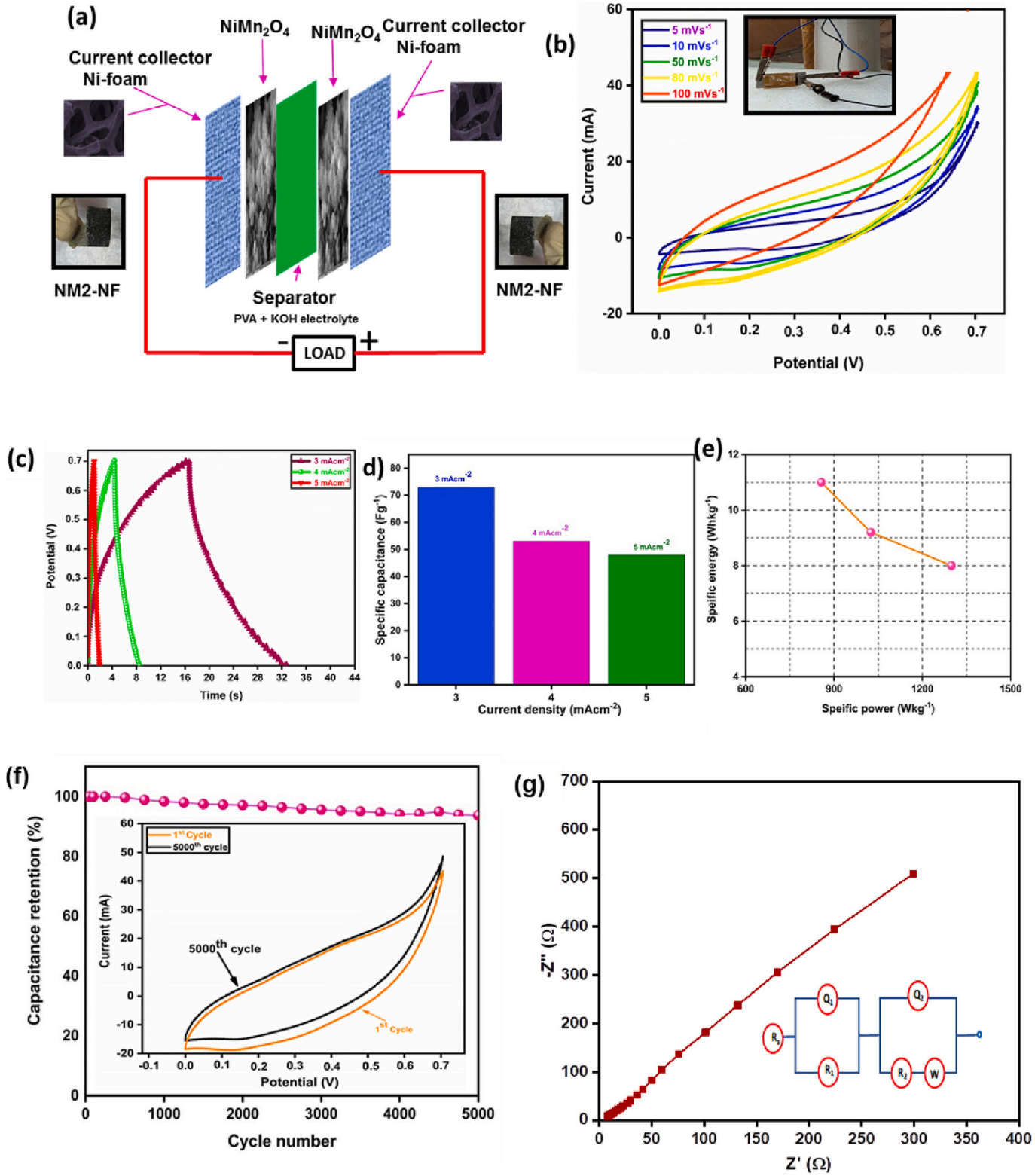

Fig. 8. Electrochemical performances of the symmetric supercapacitor device: (a) Schematic illustration of SSCs device (b) CV curves (inset: b actual photograph of the SSCs device); (c) GCD curves, (d) Specific capacitance vs. current density, (e) Ragone plot, and (f) Chemical cyclic stability of the SSCs device, (g) EIS curves.

CRediT authorship contribution statement

Suprimkumar D. Dhas: Writing – original draft, Conceptualization, Supervision. **Pragati N. Thonge:** Data curation, Investigation. **Shivaji D. Waghmare:** Writing – review & editing, Resources. **Gopal K. Kulkarni:** Visualization, Software. **Surendra K. Shinde:** Data curation. **Dae-Young Kim:** Investigation. **Teja M. Patil:** Validation. **Manesh A. Yewale:** Software, Investigation. **Annasaheb V. Moholkar:** Funding acquisition. **Daewon Kim:** Writing – review & editing.

Declaration of competing interest

The authors declare that they have no known competing financial interests or personal relationships that could have appeared to influence the work reported in this paper.

Data availability

No data was used for the research described in the article.

Acknowledgements

The authors, Dr. Suprimkumar D. Dhas and Pragati N. Thonge, are thankful to the Chhatrapati Shahu Maharaj Research Training and Human Development Institute (SARTHI), Pune, Maharashtra, for providing funding for this project. Additionally, Shri Shivaji Mahavidyalaya, Barshi, is also acknowledged by all of the authors.

References

[1] J. Zhao, A.F. Burke, Review on supercapacitors: technologies and performance evaluation, J. Energy Chem. 59 (2021) 276–291, https://doi.org/10.1016/j.jechem.2020.11.013.
[2] X. Zhao, L. Mao, Q. Cheng, J. Li, F. Liao, G. Yang, L. Xie, C. Zhao, L. Chen, Two-dimensional spinel structured co-based materials for high performance supercapacitors: a critical review, Chem. Eng. J. 387 (2020), 124081, https://doi.org/10.1016/j.cej.2020.124081.
[3] J. Johnson William, I. Manohara Babu, G. Muralidharan, Nickel bismuth oxide as negative electrode for battery-type asymmetric supercapacitor, Chem. Eng. J. 422 (2021), 130058, https://doi.org/10.1016/j.cej.2021.130058.
[4] M.E. Sahin, F. Blaabjerg, A. Sangwongwanich, A review on supercapacitor materials and developments, Turkish, J. Mater. 5 (2020) 10–24.
[5] S. Liu, S.C. Lee, U.M. Patil, C. Ray, K.V. Sankar, K. Zhang, A. Kundu, S. Kang, J. H. Park, S. Chan Jun, Controllable sulfuration engineered NiO nanosheets with enhanced capacitance for high-rate supercapacitors, J. Mater. Chem. A 5 (2017) 4543–4549, https://doi.org/10.1039/c6ta11049e.
[6] S. Karthikeyan, B. Narenthiran, A. Sivanantham, L.D. Bhatlu, T. Maridurai, Supercapacitor: evolution and review, Mater. Today Proc. 46 (2020) 3984–3988, https://doi.org/10.1016/j.matpr.2021.02.526.
[7] R. Liang, Y. Du, P. Xiao, J. Cheng, S. Yuan, Y. Chen, J. Yuan, J. Chen, Transition metal oxide electrode materials for supercapacitors: a review of recent developments, Nanomaterials. 11 (2021) 2112, https://doi.org/10.3390/nano11051248.
[8] A. Galal, H.K. Hassan, N.F. Atta, T. Jacob, Effect of redox electrolyte on the specific capacitance of $SrRuO_3$-reduced grapheme oxide nanocomposites, J. Phys. Chem. C 122 (2018) 11641–11650, https://doi.org/10.1021/acs.jpcc.8b02068.
[9] E. Elanthamilan, A. Sathiyan, S. Rajkumar, E.J. Sheryl, J.P. Merlin, Polyaniline based charcoal/Ni grapheme sites material for high performance supercapacitors, Sustain. Energy Fuels 2 (2018) 811–819, https://doi.org/10.1039/c7se00490g.
[10] K. Jeyalakshmi, S. Vijayakumar, S. Nagamuthu, G. Muralidharan, Effect of annealing temperature on the supercapacitor behaviour of β-V_2O_5 thin films, Mater. Res. Bull. 48 (2013) 760–766, https://doi.org/10.1016/j.materresbull.2012.11.054.
[11] M.S. Park, J. Kim, K.J. Kim, J.W. Lee, J.H. Kim, Y. Yamauchi, Porous nanoarchitectures of spinel-type transition metal oxides for electrochemical energy storage systems, Phys. Chem. Chem. Phys. 17 (2015) 30963–30977, https://doi.org/10.1039/c5cp05936d.
[12] Y. Zhang, L. Li, H. Su, W. Huang, X. Dong, Binary metal oxide: advanced energy storage materials in supercapacitors, J. Mater. Chem. A 3 (2015) 43–59, https://doi.org/10.1039/c4ta04996a.
[13] Z. Wu, Y. Zhu, X. Ji, $NiCo_2O_4$-based materials for electrochemical supercapacitors, J. Mater. Chem. A 2 (2014) 14759–14772, https://doi.org/10.1039/c4ta02390k.
[14] M.B. Askari, P. Salarizadeh, Binary nickel ferrite oxide ($NiFe_2O_4$) nanoparticles coated on reduced grapheme oxide as stable and high-performance asymmetric supercapacitor electrode material, Int. J. Hydrog. Energy 45 (2020) 27482–27491, https://doi.org/10.1016/j.ijhydene.2020.07.063.
[15] B. Liu, B. Liu, Q. Wang, X. Wang, Q. Xiang, D. Chen, G. Shen, New energy storage option: toward $ZnCo_2O_4$ nanorods/nickel foam architectures for high-performance supercapacitors, ACS Appl. Mater. Interfaces 5 (2013) 10011–10017, https://doi.org/10.1021/am402339d.
[16] S. Sharifi, K. Rahimi, A. Yazdani, Highly improved supercapacitance properties of $MnFe_2O_4$ nanoparticles by MoS_2 nanosheets, Sci. Rep. 11 (2021) 1–15, https://doi.org/10.1038/s41598-021-87823-6.
[17] H. Yan, J. Cheng, Z. Bai, T. Peng, Y. Lu, J. Kim, Y. Luo, Hierarchical crumpled $NiMn_2O_4$@MXene composites for high rate ion transport electrochemical supercapacitors, Dalton Trans. 50 (2021) 9827–9832. https://doi.org/10.1039/D1DT01351C.
[18] L. Li, H. Hu, S. Ding, Facile synthesis of ultrathin and perpendicular $NiMn_2O_4$ nanosheets on reduced grapheme oxide as advanced electrodes for supercapacitors 05, 2018, pp. 1714–1720, https://doi.org/10.1039/C8QI00121A.
[19] S.D. Dhas, P.S. Maldar, M.D. Patil, S.A. Mane, M.R. Waikar, R.G. Sonkawade, A. V. Moholkar, Fabrication of efficient electrochemical capacitors rooted in sol-gel derived $NiMn_2O_4$ nanoparticles, J. Electroanal. Chem. 21 (2021), 115548, https://doi.org/10.1016/j.jelechem.2021.115548.
[20] M.R. Kim, R.M. Kalla, S. Kim, M. Kim, I., Kim $NiMn_2O_4$ nano-sheet decorated hierarchically porous polyaromatic carbon spheres for high-performance supercapacitors, ChemElectroChem 4 (2017) 1214–1221, https://doi.org/10.1002/celc.201700023.
[21] Z. Wang, Z. Zhu, C. Zhang, C. Xu, C. Chen, Facile synthesis of reduced graphene oxide/$NiMn_2O_4$ nanorods hybrid materials for high-performance supercapacitors, Electrochim. Acta 230 (2017) 438–444, https://doi.org/10.1016/j.electacta.2017.02.023.
[22] K.V. Sankar, S. Surendran, K. Pandi, A.M. Allin, V.D. Nithya, Y.S. Lee, R. Kalai Selvan, Studies on the electrochemical intercalation/de-intercalation mechanism of $NiMn_2O_4$ for high, RSC Adv. 5 (2015) 27649–27656, https://doi.org/10.1039/C5RA00407A.
[23] H. Hayashi, Y. Hakuta, Hydrothermal synthesis of metal oxide nanoparticles in supercritical water, Materials 3 (2010) 3794–3817, https://doi.org/10.3390/ma3073794.
[24] L. Xiang, J. Shen, L. Lv, X. Li, S. Liu, Z. Li, $NiMn_2O_4$ nanosheet arrays with controlled mass loading as pseudocapacitor electrodes, Key Eng. Mater. 727 (2017) 678–682, https://doi.org/10.4028/www.scientific.net/KEM.727.678.
[25] S. Sahoo, S. Zhang, J. Shim, O. Nimn, Porous ternary high performance supercapacitor electrode based on, Electrochim. Acta 216 (2016) 386–396, https://doi.org/10.1016/j.electacta.2016.09.030.
[26] H. Wei, J. Wang, L. Yu, Y. Zhang, D. Hou, T. Li, Facile synthesis of NiMn2O4 nanosheet arrays grown on nickel foam as novel electrode materials for high-performance supercapacitors, Ceram. L42 (2016) 14963–14969, https://doi.org/10.1016/j.ceramint.2016.06.140.
[27] S.D. Dhas, P.S. Maldar, M.D. Patil, M.R. Waikar, R.G. Sonkawade, S.K. Chakarvarti, S.K. Shinde, D.Y. Kim, A.V. Moholkar, Probing the electrochemical properties of $NiMn_2O_4$ nanoparticles as prominent electrode materials for supercapacitor applications, Mater. Sci. Eng., B 271 (2021), 115298, https://doi.org/10.1016/j.mseb.2021.115298.
[28] U.J. Chavan, A.A. Yadav, Electrochemical behavior of spray deposited mixed nickel manganese oxide thin films for supercapacitor applications, J. Mater. Sci. Mater. Electron. 28 (2016) 2369, https://doi.org/10.1007/s10854-016-6148-z.
[29] J. Bhagwan, S. Rani, V. Sivasankaran, K.L. Yadav, Y. Sharma, Improved energy storage, magnetic and electrical properties of aligned, mesoporous and high aspect ratio nanofibers of spinel-$NiMn_2O_4$, Appl. Surf. Sci. 426 (2017) 913–923, https://doi.org/10.1016/j.apsusc.2017.07.253.
[30] H. Nan, W. Ma, Z. Gu, B. Geng, X. Zhang, Hierarchical NiMn2O4@CNT nanocomposites for high-performance asymmetric supercapacitors, RSC Adv. 5 (2015) 24607–24614, https://doi.org/10.1039/C5RA00979K.
[31] S.D. Dhas, P.S. Maldar, M.D. Patil, A.B. Nagare, M.R. Waikar, R.G. Sonkawade, A. V. Moholkar, Synthesis of NiO nanoparticles for supercapacitor application as an efficient electrode material, Vacuum 181 (2020), 109646, https://doi.org/10.1016/j.vacuum.2020.109646.
[32] S. Vijayakumar, S. Nagamuthu, G. Muralidharan, Supercapacitor studies on NiO nano flakes synthesized through a microwave route, ACS Appl. Mater. Interfaces 5 (2013) 2188–2196, https://doi.org/10.1021/am400012h.
[33] S.D. Dhas, P.S. Maldar, M.D. Patil, M.R. Waikar, R.G. Sonkawade, A.V. Moholkar, Sol-gel synthesized nickel oxide nanostructures on nickel foam and nickel mesh for a targeted energy storage application, J. Energy Storage 47 (2022) 103658. https://doi.org/10.1016/j.est.2021.103658.
[34] L. Zu, W. Zhang, L. Qu, L. Liu, W. Li, A. Yu, D. Zhao, Mesoporous materials for electrochemical energy storage and conversion 10, 2020, 2002152, https://doi.org/10.1002/aenm.202002152.
[35] Y. Ouyang, Y. Feng, H. Zhang, L. Liu, Y. Wang, Designing sandwiched and crystallized $NiMn_2O_4$/C arrays for enhanced sustainable electrochemical energy storage, ACS Sustain. Chem. Eng. 5 (2017) 196–205, https://doi.org/10.1021/acssuschemeng.6b01249.
[36] S.D. Dhas, P.S. Maldar, M.D. Patil, K.M. Hubali, U.V. Shembade, S.B. Abitkar, M. R. Waikar, R.G. Sonkawade, G.L. Agawane, A.V. Moholkar, Hydrothermal synthesis of mesoporous $NiMnO_3$ nanostructures for supercapacitor application: effect of electrolyte, J. Energy Storage 35 (2021), 102277, https://doi.org/10.1016/j.est.2021.102277.
[37] M.R. Waikar, A.S. Rasal, N.S. Shinde, S.D. Dhas, A.V. Moholkar, M.D. Shirsat, S. K. Chakarvarti, R.G. Sonkawade, Electrochemical performance of polyaniline based symmetrical energy storage device, Mater. Sci. Semicond. Process. 120 (2020), 105291, https://doi.org/10.1016/j.mssp.2020.105291.

[38] A. Sarkar, A.K. Chakraborty, S. Bera, S. Krishnamurthy, Novel hydrothermal synthesis of CoS2/MWCNT nanohybrid electrode for supercapacitor: a systematic investigation on the influence of MWCNT, J. Phys. Chem. C 122 (2018) 18237–18246, https://doi.org/10.1021/acs.jpcc.8b04137.

[39] M. Sandhiya, K. Subramani, M. Sathish, Augmenting the electrochemical performance of $NiMn_2O_4$ by doping of transition metal ions and compositing with rGO, J. Colloid Interface Sci. 598 (2021) 409–418, https://doi.org/10.1016/j.jcis.2021.04.023.

[40] M. Zhang, S. Guo, L. Zheng, G. Zhang, Z. Hao, Preparation of NiMn2O4 with large specific surface area from an epoxide-driven sol-gel process and its capacitance, Electrochim. Acta 87 (2013) 546–553, https://doi.org/10.1016/j.electacta.2012.09.085.

[41] B.N.V. Krishna, J. Bhagwan, J.S. Yu, Sol-gel routed $NiMn_2O_4$ nanofabric electrode materials for tissue paper, J. Electrochem. Soc. 166 (2019) 1950–1955, https://doi.org/10.1149/2.0661910jes.

[42] A. Ray, M. Ghosh, J.A. Ramos-ramón, S. Saha, Umapada Pal, Swapan Kumar Bhattacharya, Sachindranath Das, Study on charge storage mechanism in working electrodes fabricated by sol- gel derived spinel NiMn2O4 nanoparticles for supercapacitor application, Appl. Surf. Sci. 463 (2019) 513–525, https://doi.org/10.1016/j.apsusc.2018.08.259.

[43] B.N. Vamsi Krishna, J. Bhagwan, J. Yu, Sol-gel routed NiMn2O4 nanofabric electrode materials forSupercapacitors, ECS 10 (2019) 166, https://doi.org/10.1149/2.0661910jes.

[44] Y. Sun, J. Zhang, X. Sun, N. Huang, High-performance spinel NiMn2O4 microspheres self-assembled with nanosheets by microwave-assisted synthesis for supercapacitors, CrystEngComm. 22 (2020) 1645–1652, https://doi.org/10.1039/c9ce01623f.

[45] S. Periyasamy, P. Subramanian, E. Levi, D. Aurbach, A. Gedanken, A. Schechter, Exceptionally active and stable spinel nickel manganese oxide electrocatalysts for urea oxidation reaction 8, 2016, pp. 12176–12185, https://doi.org/10.1021/acsami.6b02491.

[46] M.Y. Arsent, N.Y. Koval, A.V. Shmigel, P.A. Tikhonov, M.V. Kalinina, NiMn2O4 spinel as a material for supercapacitors with a pseudo capacity effect, Glas. Phys. Chem. 43 (2017) 376–379, https://doi.org/10.1134/S1087659617040022.

[47] H. Pang, J. Deng, S. Wang, S. Li, J. Du, J. Chena, J. Zhang, Facile synthesis of porous nickel manganite materials and their morphology effect on electrochemical properties, RSC Adv. 2 (2012) 5930–5934, https://doi.org/10.1039/c2ra20245j.